# Simplified equations for lower crustal flow driven by lateral pressure gradients

## Jonathan Perry-Houts, 1,2 and Eugene Humphreys 1

- <sup>1</sup>Department of Earth Sciences, University of Oregon, Eugene.
- <sup>2</sup>Department of Earth and Planetary Sciences, University of California, Davis.

27 March 2021

#### **SUMMARY**

Evidence from seismology, geology, and geodynamic studies suggests that regional-scale lower crustal flow occurs in many tectonic settings. Pressure gradients caused by mantle processes and crustal density heterogeneity can provide driving force for lower crustal flow. Numerically modeling such flow can be computationally expensive. However, by exploiting symmetry in the physical system, it is possible to represent the vertical component of flow in terms of its lateral components, thereby reducing the problem's spatial dimension by one. Here we present a mathematical formulation for flow in a viscous channel below an elastic upper plate, which is optimized for solution by common numerical methods. Our formulation drastically reduces the computational load required to simulate lower crustal flow over large areas and long time scales. We apply this model to two example problems, with and without an elastic upper plate, identifying combinations of parameters that are capable of generating measurable geologic uplift.

**Key words:** Dynamics of lithosphere and mantle; Numerical approximations and analysis; Composition and structure of the continental crust

#### 1 INTRODUCTION

Metamorphic rocks derived from the middle and lower crust are often highly deformed. The net strain of the viscous crust must keep pace with the surface tectonic deformation of faulted crust, and where rock viscosity is low, significant additional flow may be driven by existing pressure gradients. Laboratory experiments for viscous deformation of crustal rock find a strong dependence on mineralogy, temperature, presence of melt or a vapor phase, and rock fabric (Shinevar et al. 2015; Strehlau & Meissner 1987; Treagus 2002; Vanderhaeghe & Teyssier 2001). Additional information on crustal flow is derived from studies of seismic anisotropy (Christensen 1972; Lin et al. 2011; Castellanos et al. 2020), tectonic behavior (Whitney et al. 2013; Stockmal et al. 1986; Clark & Royden 2000), and lithospheric foundering (Morency & Doin 2004; Wang & Currie 2017; Göğüş & Ueda 2018). Most of these studies, however, do not provide strong constraint on strain magnitude.

A variety of situations can create conditions necessary for crustal flow. Crustal motion beneath an ideal transform creates no change in crustal thickness and no lateral variation in pressure occurs (Savage 2000). In contrast, zones with tectonically forced convergence result in crustal thickening and corresponding elevated crustal pressure (e.g. Jamieson & Beaumont 2013). This pressure will tend to drive crustal flow away from areas of thickened crust. Lower crustal defor-

mation is then a combination of tectonically forced thickening and a thinning driven by this zone of elevated pressure. In an opposite fashion, low pressure beneath an extending core complex will drive lower crust to flow into the zone of thinning crust (Block & Royden 1990; Kruse et al. 1991; Rey et al. 2009). Finally, any event that locally alters lower crustal pressure will drive lower crustal flow even in absence of externally driven tectonics. Examples include: foundering of lower crust, creating a pressure drop (e.g., southern Sierra Nevada [Le Pourhiet et al. 2006] and Wallowa Mountains [Wang & Currie 2017]) magmatic crustal inflation, creating a pressure increase (McQuarrie & Rodgers 1998); delamination of mantle lithosphere, creating a pressure increase due to dynamic uplift (Göğüş & Pysklywec 2008); and other forms of mantle loading (e.g., sub-lithospheric load [Castellanos et al. 2020]). Perhaps the strongest observational constraint on crustal flow comes from observations involving rapid and well-dated modification to crustal density structure.

In the examples given above, a Poiseuille-like lower crustal channel flow is established by the geologically created pressure gradients. Below, we develop a formulation to model the evolution of this flow in two or three dimensions by integrating over depth to reduce the problem to a respective one or two dimensions. Our approach assumes lower crustal flow is locally Poiseuille (parabolic) in cross

2

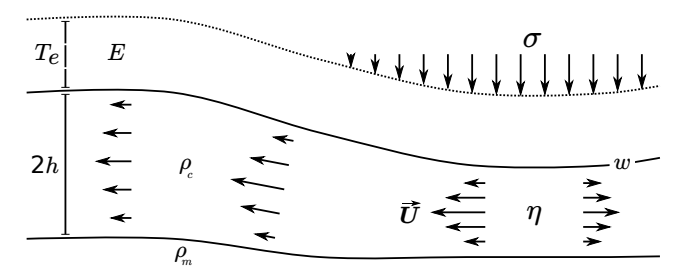


Figure 1. Schematic cross section of the "waterbed" model for lower crustal flow. We model the lower crust as a layer of Newtonian fluid with thickness 2h, overlain by an elastic plate that is warped by displacement w, under an applied overburden load,  $\sigma$ . Material properties are considered, including: effective elastic thickness,  $T_e$ , and Young's modulus, E, of the elastic upper crust; viscosity of the lower crust,  $\eta$ ; and density of the mantle and lower crust,  $\rho_m$  and  $\rho_c$ , respectively.

section, but allows spatially variable channel thickness and crustal viscosity.

We use our formulation for lower crustal flow in two test examples. First, we model the 2-D flow excited by an infinite-length tabular load, producing a transient epeirogenic response. Our second example is a 3-D model of lower crustal flow excited along a continental hot spot track. This example is motivated by the well-documented evolution of the Snake River Plain (McQuarrie & Rodgers 1998). Hot spot tracks afford good timing constraints on the changing crustal load, and on the crustal deformation and uplift at different ages since the hot spot passed.

## 2 "WATERBED" MODEL FOR LOWER CRUSTAL FLOW

We consider two-layer crust floating isostatically on an inviscid mantle, as shown in Fig. 1. The upper crust is an elastic plate, and the lower crust is a viscous channel. Variable load is applied from above, representing heterogeneity within the upper layer.

To eliminate dependence of the z direction, we assume that state variables do not vary with depth, and that lateral velocity of lower crustal flow is zero at the channel boundaries, implying a parabolic (plane Poiseuille) flow profile. These assumptions enable us to parameterize Stokes equations based on channel thickness and mid-plane flow velocity, reducing the spatial dimension of the mathematical formulation by one.

#### 2.1 Derivation

It is useful to conceptually divide the crustal flow model into two subsystems: flexurally-supported isostastic balance, and viscous fluid flow. The two components are coupled through dynamic pressure within the lower crust. We will present them separately for the purpose of demonstration, although coupling between the two subsystems requires that we consider them simultaneously when implementing numerical solvers.

#### 2.1.1 Isostasy & Flexure

To understand pressure in the lower crust, we need to balance forces acting on both the upper and lower boundaries of the channel. Each is acted upon by different applied forces, and both include variations in pressure within the lower crust.

The upper boundary is acted on by three external forces: stress due to elastic deformation of the upper plate, gravitational potential of the topographic load, and overburden applied by upper crustal heterogeneity and sedimentary deposits.

We use a classical thin plate model (Reddy 2006) for elastic stress in the upper crust, in which elastic displacement is related to the plate's material properties, geometry, and applied stress, by the relationship

$$\nabla^4 w = \frac{q}{D},\tag{1}$$

where q is an arbitrary applied load, w is plate displacement away from neutral, and D is flexural rigidity, defined as

$$D = \frac{ET_{e'}^3}{12(1-\nu^2)},\tag{2}$$

for Young's modulus E, effective elastic thickness  $T_e$ , and Poisson's ratio  $\nu$ .

Stress felt by the bending elastic plate is a combination of lithostatic stress due to topographic load,  $\rho_c gw$ , and applied overburden, sigma. Therefore, the upper boundary of the channel is described by the force balance,

$$D\nabla^4 w + \rho_c g w + \sigma = P, (3)$$

where P represents deviations in lower crustal pressure.

Equivalently, the channel's lower boundary, which represents the Moho interface, experiences stress proportional to its own relief, which is balanced by the channel's dynamic pressure,

$$(\rho_m - \rho_c)gZ_m = -P \tag{4}$$

where  $Z_m$  is elevation of the Moho. An elevated Moho must be balanced by negative dynamic pressure within the channel, and vice versa.

Moho elevation can be expressed in terms of existing variables, noting that by definition it lies below the channel's upper boundary w, separated by the lower crustal thickness 2h:

$$Z_m = w - 2h. (5)$$

Force balance for the lower channel boundary can then be written

$$P = (\rho_m - \rho_c)g(2h - w). \tag{6}$$

Combining equations (3) and (6), we express the full isostatic force balance in our system as

$$\boxed{D\nabla^4 w + \rho_m g w + 2(\rho_c - \rho_m)gh = -\sigma.}$$
 (7)

#### 2.1.2 Flow

The remaining components of our model govern the viscous flow field itself. We represent the lower crustal channel using

a Newtonian Stokes model. Beginning with a general statement of momentum balance in the absence of internal body forces,

$$\nabla \cdot \underline{\tau} = 0, \tag{8}$$

for stress tensor  $\tau$ . Vectors are expressed in boldface, and second-order tensors are underlined.

Assuming an incompressible Newtonian fluid, stress can be expressed as a linear function of differential viscous shear and isotropic pressure,

$$\underline{\tau} = \eta \underline{\dot{\varepsilon}}(\mathbf{u}) - P\underline{\mathbb{I}},\tag{9}$$

for pressure P, viscosity  $\eta,$  identity tensor  $\underline{\mathbb{I}},$  and symmetric strain rate  $\underline{\dot{\varepsilon}}$ , and fluid velocity **u**. Strain rate is a function of gradients in flow velocity:

$$\underline{\dot{\varepsilon}} = \frac{1}{2} \left[ \nabla \mathbf{u} + (\nabla \mathbf{u})^T \right]. \tag{10}$$

In an incompressible fluid, continuity requires zero divergence in the flow field,

$$\nabla \cdot \mathbf{u} = 0. \tag{11}$$

Combining equations (8)–(11), our flow laws can be rewrit-

$$\nabla \cdot (\eta \nabla \mathbf{u}) - \nabla P = 0 \tag{12}$$

$$\nabla \cdot \mathbf{u} = 0. \tag{13}$$

Assuming the viscosity field is smooth relative to flow  $(\nabla \eta \ll 1)$ , we can bring it outside the derivative in equation (12), and expand the governing equations to index notion,

$$\eta (u_{x,x,x} + u_{x,y,y} + u_{x,z,z}) - P_{,x} 
\eta (u_{y,x,x} + u_{y,y,y} + u_{y,z,z}) - P_{,y} 
\eta (u_{z,x,x} + u_{z,y,y} + u_{z,z,z}) - P_{,z}$$
(14)

$$u_{x,x} + u_{y,y} + u_{z,z} = 0, (15)$$

where subscripts represent vector component indices, and commas indicate derivatives with respect to the following index.

We now introduce the constraints that viscosity is constant with depth, and that lateral velocity goes to zero at the top and bottom of the lower crustal channel. These constraints require that the flow field follows a parabolic profile with respect to depth. Using a layer-centered coordinate system allows us to take advantage of the inherent symmetry present in the system. We can therefore uniquely express the 3-dimensional flow in terms of a 2-dimensional vector field **U**, where  $u_i(z=0) = U_i$ ,

$$u_{i\in\{x,y\}} = \left(1 - \frac{z^2}{h^2}\right) U_i.$$
 (16)

Substituting equation (16) into equation (15) yields

$$u_{z,x} = \left(\frac{z^2}{h^2} - 1\right) (U_{x,x} + U_{y,y}),$$
 (17)

therefore
$$u_z = \int_0^z u_{z,z} dz = \left(\frac{z^3}{3h^2} - z\right) (U_{x,x} + U_{y,y}). \tag{18}$$

The full velocity field can then be expressed in terms of  ${\bf U}$ :

$$\mathbf{u} = \begin{cases} \left(1 - \frac{z^2}{h^2}\right) & U_x \\ \left(1 - \frac{z^2}{h^2}\right) & U_y \\ \left(\frac{z^3}{3h^2} - z\right) & (U_{x,x} + U_{y,y}) \end{cases}$$
(19)

Substituting equations (6) and (19) into (12), and evaluating the solution at z = 0, our governing flow laws reduce

$$\left[ \eta \nabla^2 \mathbf{U} - \frac{2\eta}{h^2} \mathbf{U} + (\rho_m - \rho_c) g \nabla(w - 2h) = 0 \right]$$
 (20)

#### 2.1.3 Time dependence

Time dependence enters the system through lower crustal thickening and thinning. Solving equation (18) at the upper channel boundary, we find

$$\dot{h} \equiv \frac{\partial h}{\partial t} = u_z(z=h) = -\frac{2}{3}h\left(\nabla \cdot \mathbf{U}\right).$$
 (21)

Additional time dependence can be introduced by variations in the overburden load  $(\sigma)$ , but we treat the applied load as an independent variable, and not a coupled component of our system of equations.

#### 2.1.4 Scaling

Nondimensionalization narrows the parameter space of our problem, eliminating redundancy when testing suites of multiple models. Scaling has the added benefit of coercing the system of equations into a form that is more well conditioned, and thus more efficiently solved by iterative linear solver schemes, as discussed in Appendix A1.4.

We scale our model in terms of representative values: channel thickness  $h_0$ , distance  $L_0$ , viscosity  $\eta_0$ , pressure  $P_0$ , and strain rate  $\dot{\varepsilon}_0$ . All variables and operators can then be replaced by their dimensionless equivalents, indicated by a prime (') superscript:  $x_i = L_0 x_i', h = h_0 h', \nabla = L_0^{-1} \nabla', \eta = \eta_0 \eta', P = P_0 P', U = h_0 \dot{\varepsilon}_0 U', g = \dot{\varepsilon}_0^2 h_0 g', D = P_0 L_0^3 D', w = h_0 w', \sigma = P_0 \sigma', \rho_m = P_0 (h_0 \dot{\varepsilon}_0)^{-2} \rho'_m,$ and  $\rho_c = P_0 (h_0 \dot{\varepsilon}_0)^{-2} \rho'_c$ .

We arrange our governing equations in terms of two dimensionless parameters:

$$\Pi = \frac{P_0}{\eta_0 \dot{\varepsilon}_0}, \qquad (22)$$

$$\gamma = \frac{h_0}{L_0}. \qquad (23)$$

$$\gamma = \frac{h_0}{L_0}. (23)$$

Equations (7), (20), and (21) can then be written

$$\gamma D' \nabla'^4 w' + \rho'_m g' w' + 2(\rho'_c - \rho'_m) g' h' = -\sigma', \qquad (24)$$

$$\eta' \nabla'^2 \mathbf{U}' - \frac{2\eta'}{\gamma h'^2} \mathbf{U}'$$

$$+\Pi(\rho'_m - \rho'_c)g'\nabla'(w' - 2h') = 0, \tag{25}$$

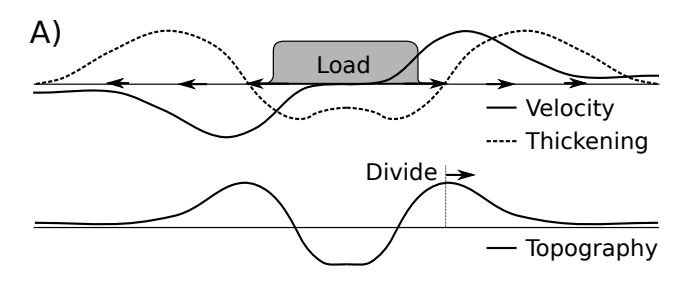
$$\frac{dh'}{dt'} + \gamma \frac{2}{3}h'(\nabla' \cdot \mathbf{U}') = 0. \tag{26}$$

#### EXAMPLE MODELS

#### 3.1 Two-dimensional model of time evolving flow

An exceptionally useful "natural experiment" is the creation and development of continental hot spot tracks. These systems create a propagating heat source coincident with emplacement of mid-crustal load. The dynamic response occurs in a setting where crustal thickness and topographic

### 4 J. Perry-Houts and E. Humphreys



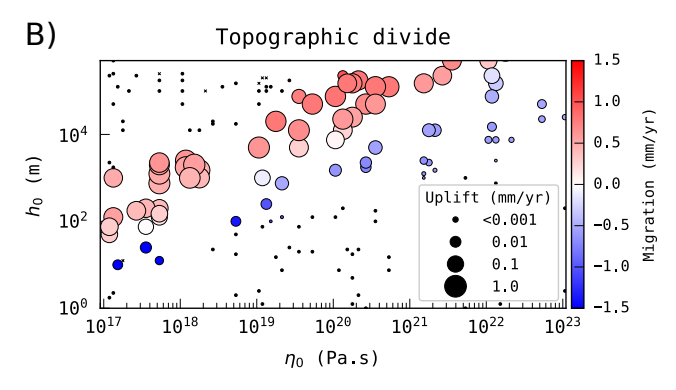


Figure 2. Epeirogenic transients resulting from forced flow in an isoviscous lower crust with no overlying elastic plate, as illustrated in panel  ${\bf A}$ . A transient pulse of crustal thickening produces long-wavelength epeirogeny that migrates over time. The speed at which this topographic bulge travels depends most strongly on the channel's viscosity and thickness. A Monte Carlo suite of models is presented in panel  ${\bf B}$ , with warm colors representing movement away from the applied load, and cool colors indicating motion towards the load. Marker size indicates the peak uplift rate reached during the course of the model, and models in which no well-defined isolated uplift is detected are indicated with an  $\times$ .

evolution can be compared to the pre-hot spot crustal and stratigraphic references.

Seismic imaging and gravity studies show that Yellowstone's Snake River Plain (SRP) contains an approximately 17km thick mid-crustal sill, overlain by about 5km of sedimentary and volcanic basin fill. McQuarrie & Rodgers (1998) propose that the SRP's seismically-active periphery, characterized by high topography (the so-called "tectonic parabola"), is a result of accumulated lower crust that has been ejected from below the SRP. Using results obtained by Kruse et al. (1991) for the Basin and Range, they estimate that in order to produce uplift on the length and time scales applicable to the SRP, the lower crust must have a viscosity of approximately 10<sup>17</sup>.

We construct a simple cross-sectional model using length, mass, and time scales consistent with prior studies (McQuarrie & Rodgers 1998; Yuan et al. 2010). Our model domain is 2,000km wide, with overburden stress  $\sigma=150 \mathrm{MPa}$  applied to a 100km region at its center. The model runs over 10My of simulated time. For comparison with prior studies, we omit elastic strength of the upper crust, setting D=0.

We run a Monte Carlo suite of similar models, varying only viscosity and initial thickness of the lower crust. This allows us to quantify the maximum surface uplift attained during each model run, and the rate at which the location of peak topography translates over time. Fig. 2 demonstrates

conditions under which lower crustal flow can produce dramatic changes in topography. These results are consistent with prior studies, indicating a relatively narrow range of parameter space in which the SRP's observed 0.1–1mm/yr uplift rates are possible.

McQuarrie & Rodgers (1998) interpreted similar evidence as a constraint on Idaho's lower crustal viscosity. However, the presence of an elastic upper plate likely plays a significant role in shaping uplift around the SRP. Further work is required to make definitive interpretations about the nature of Yellowstone's tectonic parabola. Our method provides means by which these prior studies can be extended to more realistic scenarios, including the presence of an elastic upper crust, and expansion to 3 dimensions.

## 3.2 Three-dimensional model of time evolving flow with a propagating load

As a demonstration of the full capabilities of our model, we present a fully 3-dimensional time-dependent model of lower crustal flow beneath an elastic upper plate. Parameters are chosen based on the model suite in section 3.1. Using a model domain representing a square map area 2,000km  $\times$  2,000km, we select representative quantities  $h_0 = 5$ km, and  $\eta_0 = 10^{20}$ Pa.s. Unlike the previous example, we incorporate an elastic upper plate with Young's modulus E = 70GPa, elastic thickness  $T_e = 12$ km, and Poisson's ratio  $\nu = 0.25$ .

Applied overburden stress in this model is meant to approximate the geometry and magnitude of mid-crustal magmatic intrusions along a continental hot spot track, including sedimentary deposition within the subsided regions. Overburden is added within a 100km-wide disk that propagates across the model domain at 10cm/yr. A dense load is left behind with a maximal magnitude of 150MPa, consistent with the stress estimated by McQuarrie & Rodgers (1998) for the eastern Snake River Plain.

Fig. 3 shows the resulting topography predicted by this model after 5My. A prominent "wake" of topographic uplift is generated, running parallel with the path of hot spot propagation. An arcuate region of uplift precedes arrival of the emplaced load by approximately 100km, mostly owing to the flexural strength of the upper plate. Animations of these model results with alternate views, as well as all necessary code and documentation to reproduce these models are included in the online supplement to this paper.

#### 4 DISCUSSION

#### 4.1 Interpretation

The modeling framework presented here has several advantages in terms of both efficiency and predictive power. Scaling parameters introduced in section 2.1.4 can be powerful tools for quantifying unconstrained properties of the crust and lithosphere.

While  $\gamma$  is easily visualized as a physical aspect ratio of the viscous channel,  $\Pi$  is not directly comparable to any common or obvious dimensionless quantity. In more well established terms, it can be expressed as a ratio between the

fluid mechanical Bejan number, and the Reynolds number,

$$\Pi = (Be)(Re^{-1}) = \left(\frac{\rho h^2 P}{\eta^2}\right) \left(\frac{\eta}{\rho h U}\right) = \frac{P}{\eta \dot{\varepsilon}}$$
 (27)

This combination is most easily interpreted as the ratio between length scales of momentum diffusion and momentum advection. In our case,  $\Pi^{-1}$  conceptually corresponds to the ability of viscosity to support gradients in crustal thickness. Systems where  $\Pi << 1$  are capable of sustaining substantial topographic relief at both the surface and Moho, and solitary pulses of crustal thickening can be more pronounced. Systems where  $\Pi >> 1$  will more quickly adjust to pressure gradients, and pulses of crustal thickening will be more diffusive.

Similarly, large  $\gamma$  values are associated with diffusive behavior, while low  $\gamma$  values restrict and localize flow, enabling sharp gradients in crustal thickness. Effects of variations in each parameter are demonstrated in Fig. 2, where the x-axis corresponds to  $\Pi^{-1}$ , and the y-axis to  $\gamma$ .

Dimensional analysis using  $\Pi$  and  $\gamma$  becomes less effective in the presence of an elastic upper crust. Models with substantial elastic strength may be dominated by the upper plate's preferred flexural wavelength, rather than the viscously-supported transient uplift demonstrated in section 3.1.

The time-dependent model described in section 3.2 illustrates this effect, where the peripheral bulges lie parallel to the path of propagating intrusion, indicating that the location of uplift does not shift substantially over time. Flexurally-dominated models can also adjust instantaneously over long distances to localized changes in overburden. This can generate features like the arcuate bulge 'upstream' of the propagating magmatic center, even in cases where the overburden load moves substantially faster than the crustal flow itself.

#### 4.2 Efficiency

The modeling method presented here is based on the principle that lower dimensional models are inherently more efficient than their higher dimensional equivalent. This is true for two primary reasons: the inherent reduction in numerical complexity afforded by requiring fewer mesh nodes, and reduced reliance on complexities like deformed mesh topology or high viscosity gradients. Both of these considerations has caveats that make the comparison slightly more complex.

While the specifics of any particular model comparison can vary, it's obvious that a 2D model has fewer mesh nodes, and therefore fewer numerical degrees of freedom, than a 3D model spanning the same spatial distances with equal resolution. Stated differently, increasing the spatial dimension from 1D to 2D, for instance, will increase the number of mesh nodes by approximately a power of 2:  $\mathcal{O}(n^2)$ . Similarly, moving from 2D to 3D scales with order  $\mathcal{O}(n^{3/2})$ .

However, fewer mesh nodes does not inherently result in a simpler numerical system. In particular, it is worth noting that in order to achieve the dimensional reduction, we have added complexity to the governing equations by increasing the differential order of the system from Laplacian to biharmonic form. Ultimately, this has the effect of increasing the number of equations being solved from 2 to 4, and introducing new solution variables. Fortunately, adding equations to our system increases the number of degrees of freedom linearly,  $\mathcal{O}(n)$ , which grows much more slowly than the polynomial growth associated with increased spatial dimensions.

Further, the reduced spatial dimension eliminates a number of complexities that would otherwise prove challenging. In order to handle the changing thickness of the lower crustal channel, the traditional implementation would require either Lagrangian deformation of the upper and lower mesh boundaries, or to incorporate additional elements, including the mantle lithosphere and the upper crust. The first approach is not possible in most modeling frameworks, and doing so would require extensive customization on top of the underlying library. The second approach would introduce high viscosity contrasts between the lower crust and both confining layers. Large viscosity contrasts in fluid flow models are known to produce numerical systems that converge more slowly than isoviscous equivalents (Duretz et al. 2011).

#### 4.3 Limitations

The efficiency gained by reducing the model's spatial dimension comes at the cost of physical approximations in the model variables.

Viscosity is naturally a function of depth within the Earth's crust, contradicting our assumption of a purely parabolic flow profile. Observational constraints on the specific flow profile of the lower crust are weak, and therefore it is challenging to assess the degree to which the model assumptions hold true in any particular case. Seismic measurements provide the best measure of crustal anisotropy (Castellanos et al. 2020) but do not reveal the flow profile, only an integrated view of mineral alignment across a broad region.

For these reasons, it is best to interpret the model parameters in terms of their net impedance to flow. That is, the rate of strain accumulation integrated through the complete lower crustal column, for a given lateral pressure gradient. The model's viscosity can then be considered to represent an integrated average, enabling interpretation of our model results in the presence of non-parabolic flows. Care must be taken to scale the model parameters accordingly, as the volume flux across a heterogeneous channel differs from that of an isoviscous parabolic flow.

Our model also assumes that the lithosphere is always in a state of isostatic equilibrium. Of course there are many cases in which the lithosphere is out of isostatic equilibrium, either because of recent tectonic deformation, or because of mantle-derived vertical stresses, so called "dynamic topography."

Our assumption implies that pressure gradients are induced only by an imposed overburden stress and variations in gravitational potential energy due to thickening and thinning of the crustal column. While deriving a mathematical formulation for the contribution of non-isostatic gravitational potential energy is beyond the scope of this work, one could be formulated and implemented with very few changes to the methods presented here. Variations in mantle-derived uplift could be expressed as perturbations to the pressure field, and could be applied in practice by simply augmenting the external forcing term,  $\sigma.$ 

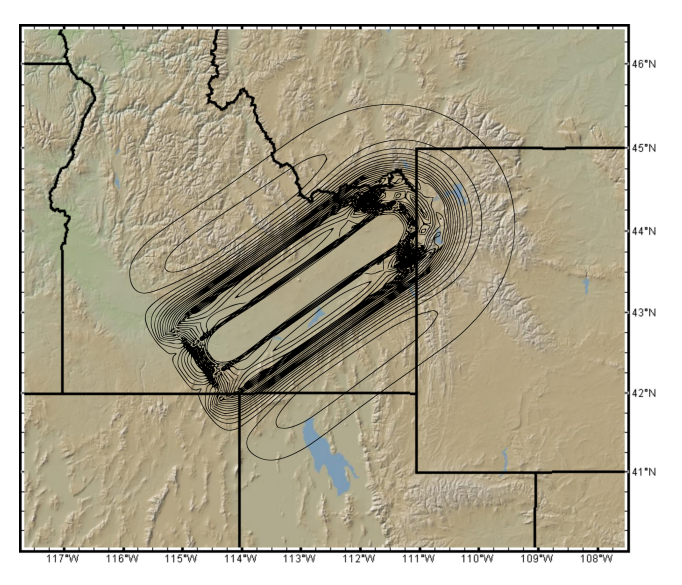


Figure 3. Simulation of lower crustal flow around the Yellowstone hot spot demonstrates the predictive power of our method for geologic systems. In this model, a propagating source of magmatic activity produces a time-evolving domain of increased overburden weight. The added load drives lower crustal flow towards the margins, resulting in a similar uplift pattern to the so-called "tectonic parabola" surrounding Yellowstone and the Snake River Plain. The black contour lines indicate surface elevations predicted by our model in 50m increments. The model's total relief spans approximately 2km, greater than the ~1km observed along the Snake River Plane. We attribute the difference to surface processes which our model does not account for. Erosion and deposition would tend to smooth the high frequency variations within the basin, reducing the overall amplitude of relief.

#### CONCLUSIONS

Opinions vary as to the importance and significance of lower crustal flow excited by the presence of intra-crustal heterogeneity. Estimation of real-world pressure gradients is straightforward and usually fairly accurate, given seismic and petrologic data about the structure of the crust. Crustal viscosity, however, is poorly constrained because of its sensitivity to variations in composition and temperature, as well as on the mineral fabric of crustal rocks. As a result, evidence for significant crustal flow comes from the interpretation of local topography, seismic imaging, and geologic mapping.

Compelling examples include core complexes (Whitney et al. 2013), the Snake River Plain (McQuarrie & Rodgers 1998), Wallowa moat (Wang & Currie 2017; Castellanos et al. 2020), and the Basin and Range (Block & Royden 1990; Kruse et al. 1991). The proposed regional-scale crustal flow from Tibet to SE Asia (Royden et al. 1997) illustrates the possible importance of this process over a distance of > 1000 km.

When considering these effects in time-evolving systems, especially when the problem is three dimensional, numerical simulations can become computationally expensive. We develop and illustrate an algorithm to efficiently model the instantaneous or time evolving lower-crustal flow in two or three dimensions for situations that may have a complex loading and rheologic structure and history.

#### 6 DATA AVAILABILITY

The data underlying this article are available in the article and in its online supplementary material. Any modifications to the supporting code made subsequent to the publication of this article will be available in its github repository at https://github.com/jperryhouts/waterbottlemodel/.

#### ACKNOWLEDGMENTS

We thank Jyotirmov Paul and an anonymous reviewer for constructive reviews that improved the quality and clarity of this paper. This work was supported by National Science Foundation grant EAR-1727451.

#### REFERENCES

Bangerth, W., Hartmann, R., & Kanschat, G., 2007. Deal.II a General Purpose Object Oriented Finite Element Library, ACM Transactions on Mathematical Software, 33(4), 24/1-24/27.

Block, L. & Royden, L. H., 1990. Core complex geometries and regional scale flow in the lower crust, Tectonics, 9(4), 557-567. Castellanos, J. C., Perry-Houts, J., Clayton, R. W., Kim, Y., Stanciu, A. C., Niday, B., & Humphreys, E., 2020. Seismic anisotropy reveals crustal flow driven by mantle vertical loading in the Pacific NW, Science Advances, 6(28), eabb0476.

Christensen, N. I., 1972. Seismic Anisotropy in the Lower

Oceanic Crust, Nature, **237**(5356), 450–451. Clark, M. K. & Royden, L. H., 2000. Topographic ooze: Building the eastern margin of Tibet by lower crustal flow, Geology, **28**(8), 703–706.

Duretz, T., May, D. A., Gerya, T. V., & Tackley, P. J., 2011. Discretization errors and free surface stabilization in the finite difference and marker-in-cell method for applied geodynamics: A numerical study, Geochemistry, Geophysics, Geosystems, **12**(7), Q07004.

Göğüş, O. H. & Pysklywec, R. N., 2008. Near-surface diagnostics of dripping or delaminating lithosphere,  $Journal\ of\ Geophysical$ Research: Solid Earth, 113(B11), B11404.

Göğüş, O. H. & Ueda, K., 2018. Peeling back the lithosphere: Controlling parameters, surface expressions and the future directions in delamination modeling, Journal of Geodynamics, **117**, 21–40.

Jamieson, R. A. & Beaumont, C., 2013. On the origin of orogens, Geological Society of America Bulletin, 125(11-12), 1671–1702. Kronbichler, M., Heister, T., & Bangerth, W., 2012. High accuracy mantle convection simulation through modern numerical methods, Geophysical Journal International, 191(1), 12-29.

Kruse, S., McNutt, M., Phipps-Morgan, J., Royden, L., & Wernicke, B., 1991. Lithospheric extension near Lake Mead, Nevada: A model for ductile flow in the lower crust, Journal of Geophysical Research: Solid Earth, 96(B3), 4435–4456.

Le Pourhiet, L., Gurnis, M., & Saleeby, J., 2006. Mantle instability beneath the Sierra Nevada Mountains in California and Death Valley extension, Earth and Planetary Science Letters, **251**(1-2), 104-119.

Lin, F.-C., Ritzwoller, M. H., Yang, Y., Moschetti, M. P., & Fouch, M. J., 2011. Complex and variable crustal and uppermost mantle seismic anisotropy in the western United States, Nature Geoscience, 4(1), 55–61.

McQuarrie, N. & Rodgers, D. W., 1998. Subsidence of a volcanic basin by flexure and lower crustal flow: The eastern Snake River Plain, Idaho, *Tectonics*, 17(2), 203-220.

Morency, C. & Doin, M.-P., 2004. Numerical simulations of the mantle lithosphere delamination, Journal of Geophysical Research: Solid Earth, 109(B3), B03410.

Reddy, J. N., 2006. Theory and Analysis of Elastic Plates and Shells, CRC Press.

Rey, P. F., Teyssier, C., & Whitney, D. L., 2009. Extension rates, crustal melting, and core complex dynamics, Geology, **37**(5), 391–394.

Royden, L. H., Burchfiel, B. C., King, R. W., Wang, E., Chen, Z., Shen, F., & Liu, Y., 1997. Surface Deformation and Lower Crustal Flow in Eastern Tibet, Science, 276(5313), 788–790.

Savage, J. C., 2000. Viscoelastic-coupling model for the earthquake cycle driven from below, Journal of Geophysical Research: Solid Earth, 105(B11), 25525-25532.

Shinevar, W. J., Behn, M. D., & Hirth, G., 2015. Compositional dependence of lower crustal viscosity, Geophysical Research Letters, 42(20), 8333-8340.

Stockmal, G. S., Beaumont, C., & Boutilier, R., 1986. Geodynamic models of convergent margin tectonics: Transition from rifted margin to overthrust belt and consequences for forelandbasin development, AAPG Bulletin, 70(2), 181–190.

Strehlau, J. & Meissner, R., 1987. Estimation of crustal viscosities and shear stresses from an extrapolation of experimental steady state flow data, Composition, Structure and Dynamics of the Lithosphere-Asthenosphere System, 16, 69-87.

Treagus, S. H., 2002. Modelling the bulk viscosity of two-phase mixtures in terms of clast shape, Journal of Structural Geology, **24**(1), 57–76.

Vanderhaeghe, O. & Teyssier, C., 2001. Crustal-scale rheological transitions during late-orogenic collapse, Tectonophysics, **335**(1-2), 211–228.

Wang, H. & Currie, C. A., 2017. Crustal deformation induced by mantle dynamics: Insights from models of gravitational lithosphere removal, Geophysical Journal International, 210(2),

Whitney, D. L., Teyssier, C., Rey, P., & Buck, W. R., 2013. Continental and oceanic core complexes, GSA Bulletin, 125(3-4), 273-298.

Yuan, H., Dueker, K., & Stachnik, J., 2010. Crustal structure and thickness along the Yellowstone hot spot track: Evidence for lower crustal outflow from beneath the eastern Snake River Plain, Geochemistry, Geophysics, Geosystems, 11(3)

#### APPENDIX A: NUMERICAL IMPLEMENTATION DETAILS

All code and documentation required to reproduce the models and convergence tests presented here can be found in the online supplement to this paper.

#### A1 Implementation

The governing equations above can be solved with a variety of techniques. Our model is implemented in C++, and based on the DEAL.II finite element library (Bangerth et al. 2007).

#### Nonlinearity

Interdependence of variables in equations (24) - (26) introduces nonlinearities which must be considered when solving the system. Our aim is to define a set of equations, which can be represented as a matrix multiplication of form

$$Mx = b, (A.1)$$

where M is a matrix of linear operators, x is a vector of solution variables, and b is a vector of source terms.

We handle nonlinearities in the governing equations by selectively substituting variables with approximated values, converging on an accurate solution through the Picard iterative method. This requires imposing initial conditions, and repeatedly updating substitution variables with values from the most recent linear solution.

Choices about which variables to solve linearly and which to iterate on, are mostly arbitrary from a mathematical perspective. We choose a combination of Picard substitutions that maximizes symmetry of our equations, thus improving stability and efficiency of the linear solver.

First, we handle time dependence of equation (26) with a backwards Euler scheme,

$$h \approx h_n + \dot{h}\Delta t,\tag{A.2}$$

for current and previous half-thickness h and  $h_n$ , respectively. Substituting equation (26) into (A.2) produces a nonlinear function, which we linearize by substituting a system variable h with an approximated solution,  $\bar{h}$ . Dropping the dimensionless 'prime' superscript notation, and rearranging terms, we express our time stepping method as

$$h + \Delta t \gamma \bar{h} \frac{2}{3} (\nabla \cdot \mathbf{U}) = h_n,$$
 (A.3)

Similarly, we introduce an approximated elastic flexure,  $\bar{w}$ , rewriting equations (24) and (25) as

$$\eta \nabla^{2} \mathbf{U} - \frac{2\eta}{\gamma \bar{h}^{2}} \mathbf{U} + 2\Pi(\rho_{c} - \rho_{m}) g \nabla h$$

$$= \Pi(\rho_{c} - \rho_{m}) g \nabla \bar{w}, \qquad (A.4)$$

$$\gamma D \nabla^{4} w + \rho_{m} g w = 2(\rho_{m} - \rho_{c}) g \bar{h} - \sigma. \qquad (A.5)$$

$$\gamma D \nabla^4 w + \rho_m q w = 2(\rho_m - \rho_c) q \bar{h} - \sigma. \tag{A.5}$$

We repeatedly solve the full system of equations during each time step, updating the substitution variables with the each new solution. This process is repeated until the solution no longer changes significantly between iterations. Convergence is measured using the  $L_2$  norm of difference between the current and previous solutions

$$||\Psi - \bar{\Psi}||_{L_2} < \epsilon, \tag{A.6}$$

for the complete solution vector  $\Psi$ , and predefined tolerance  $\epsilon$ . Tolerance values of  $\epsilon \approx 10^{-12}$  typically converge in less than 10 iterations for simple cases, as demonstrated in Fig. A1.

#### A1.2 Discretization

The finite element method offers a number of advantages to solving elliptic partial differential equations in terms of efficiency and accuracy. Further work on lower crustal flow will likely require coupling these equations with geodynamic models of mantle processes, which are frequently based on the finite element method, themselves. We therefore chose to base our implementation on DEAL.II, the finite element library underlying the popular geodynamic framework, As-PECT (Kronbichler et al. 2012).

The governing laws formulated in equations (A.3) – (A.5), can be grouped into two independent blocks, representing the subsystems defined in Sections 2.1.2 and 2.1.1. The upper left block represents the coupled equations (A.4)

8

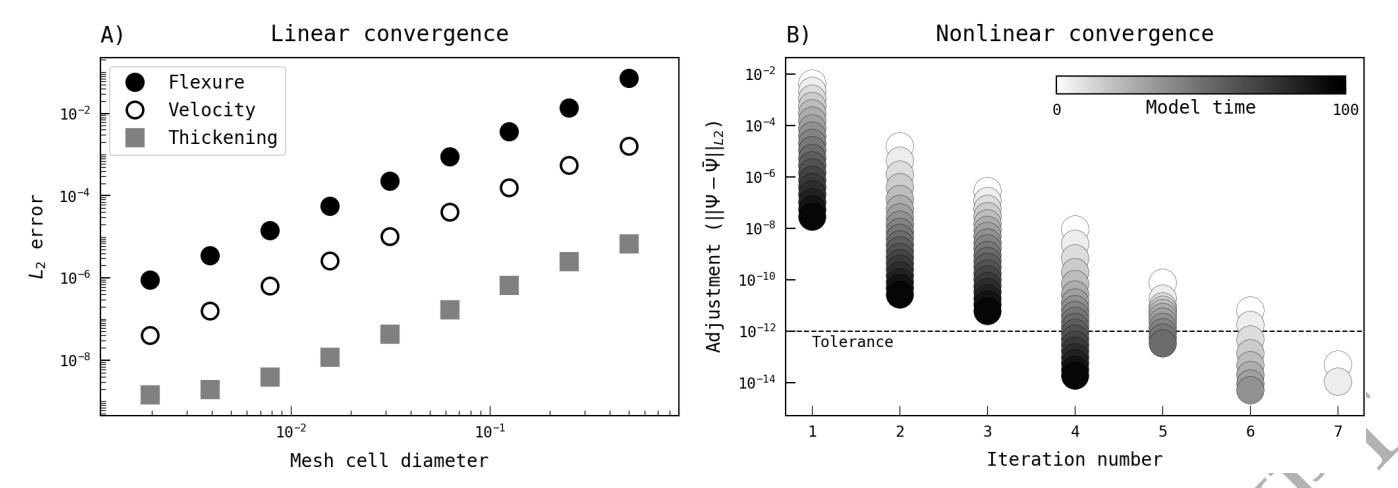


Figure A1. Numerical convergence. Panel A demonstrates convergence of our model output to a known analytic solution. Both time independent variables,  $\mathbf{U}$  and w, demonstrate the expected quadratic convergence with respect to spatial resolution. The time dependent rate of crustal thickening does not have an exact analytic solution, but our model does converge towards a first-order approximation over the initial time step. Panel B demonstrates convergence across nonlinear iterations, for multiple steps in a time-dependent model. Convergence is reached when the integrated difference between the current and previous solution falls below a predefined tolerance. Because the model presented here approaches an equilibrium configuration over time, the initial residual decreases for later time steps. Therefore, fewer nonlinear iterations are required in order to reach the desired tolerance.

and (A.3) for viscous flow, and the lower right block represents equation (A.5) for flexural isostasy.

The flow block presents a challenge for the finite element method, because of its metaharmonic form. The finite element method is not well suited to solving high order PDE's, but other methods exist to do this. The simplest approach is by way of a secondary solution variable v, splitting equation (A.5) into a "mixed" system:

$$\gamma D \nabla^2 v + \rho_m g w = 2(\rho_m - \rho_c) g \bar{h} - \sigma$$

$$v - \nabla^2 w = 0.$$
(A.8)

Both w and v can then be solved with traditional finite element formulations, using linear basis functions and Dirichlet boundary conditions.

#### $Mathematical\ symmetry$ A1.3

To improve stability and efficiency of linear solvers, it is advantageous to ensure that the operator matrix M in equation (A.1) is symmetric. Both the flexure and flow blocks of our system, as defined above, are asymmetric. However, because of our choice of Picard substitutions, they are only asymmetric in scalar coefficients and not operators. Both blocks can therefore be symmetrized by multiplying each function by appropriate coefficients.

Rearranging terms to regain symmetry leads us to the form of our equations which we ultimately implement in code:

$$-\eta \bar{h} \nabla^{2} \mathbf{U} + \frac{2\eta}{\gamma \bar{h}} \mathbf{U} + 2\Pi(\rho_{m} - \rho_{c}) g \bar{h} \nabla h$$

$$= \Pi(\rho_{m} - \rho_{c}) g \bar{h} \nabla \bar{w}, \qquad (A.9)$$

$$\Pi(\rho_{m} - \rho_{c}) g \bar{h} (\nabla \cdot \mathbf{U}) + \frac{3\Pi(\rho_{m} - \rho_{c}) g}{2\pi i \hbar} h$$

$$= \frac{3\Pi(\rho_m - \rho_c)gh_n}{2\Delta t}, \qquad (A.10)$$

$$= \frac{3\Pi(\rho_m - \rho_c)gh_n}{\gamma \Delta t}, \qquad (A.10)$$

$$\frac{\gamma D}{\rho_m g} \nabla^2 v + w = \frac{2(\rho_m - \rho_c)}{\rho_m} \bar{h} - \frac{\sigma}{\rho_m g}, \qquad (A.11)$$

$$w - \nabla^2 w = 0, \qquad (A.12)$$

resulting in a linear system of form

$$\begin{pmatrix}
\underline{A} & \underline{B}^{T} & 0 & 0 \\
\underline{B} & \underline{C} & 0 & 0 \\
0 & 0 & \underline{E} & \underline{\mathbb{I}} \\
0 & 0 & \underline{\mathbb{I}} & \underline{F}
\end{pmatrix}
\begin{pmatrix}
U \\ h \\ v \\ w
\end{pmatrix} = \begin{pmatrix}
G \\ H \\ J \\ 0
\end{pmatrix}.$$
(A.13)

It should be noted that equation (A.10) is only valid for t>0, and  $\Delta t>0$ , but because it is only an initialization step, we can impose values for h, and effectively ignore equation (A.10), moving the second term from equation (A.9) to the right hand side for that step.

#### A1.4 Solvers

The choice of linear solver method has an important impact on the efficiency and accuracy of any numerical model. Direct solvers offer the advantage of simple implementation and guaranteed convergence, while iterative solvers are more computationally efficient in most cases. The equations described in section 2.1 can be solved in their original form with a direct solver scheme, avoiding complexities of scaling and symmetrization. However, direct solvers can become very computationally expensive for 2D (pseudo-3D) models.

The governing equations described here are challenging to solve with iterative methods for a number of reasons. Notably, they are asymmetric in their original form, as is addressed in section A1.3. They are also indefinite or semi-definite in their weak form, and they tend to be ill-conditioned, with eigenvalues spread across many orders of magnitude. Fortunately, physical constraints such as h>>0 and careful scaling parameters, as described in section 2.1.4, can help ensure that our model remain well conditioned and positive definite. Lastly, depending on model parameters, it is possible to end up with zeros on the diagonal of the system matrix, which precludes the use of most common preconditioners.

An optimal solver would likely use the conjugate gradient method with a model-specific block Schur preconditioner. We will leave development of such a method for future work. Rather, we have tested a variety of generic preconditioner-solver pairs with a variety of different model setups.

Most common preconditioners are automatically precluded from use, because of the possibility of zeros existing along the system matrix diagonal. We found that an incomplete LU factorization (ILU) preconditioner works well in our test cases.

We tested a variety of solvers, including the general minimum residual method (GMRES), conjugate gradient method (CG), and biconjugate gradient stabilized method (BiCGStab). Of these, the combination of ILU preconditioner and CG solver outperformed all other options in both accuracy and efficiency.

Our model falls back to a direct solver scheme in cases where the preconditioned CG solver fails to converge. In our experience, this does happen on occasion, usually on the first nonlinear iteration of a time step. The model seems to usually recover on the subsequent iteration to a state in which the CG solver successfully converges. We have not encountered models which consistently fail to converge, given a relatively wide range of input parameters. Models which are not properly scaled may be more prone to non-convergence for the reasons discussed above.

#### A2 Validating numerical solutions

To validate that our code is accurately solving the governing equations, we perform benchmark models in 1D, comparing the results to analytically derived solutions. We generate analytical benchmarks using the method of manufactured solution. Choosing simple functions for w,  $\mathbf{U}$ , and h allows us to forward calculate forcing terms compatible with our imposed solution. Applying the resulting terms to the right hand side in our code enables direct comparison of our numerical results with the expected solution.

We begin by applying simple uniform coefficients for the state variables:  $\Pi=1, \ \gamma=1, \ \rho_m=1, \ \rho_c=0.85, \ g=1, \ D=1, \ {\rm and} \ h_{(t=0)}=1.$  We choose an analytic solution for w that will be resolvable on even very coarse meshes:

$$w = 0.1\sin(2\pi x) + 1. \tag{A.14}$$

Plugging equation (A.14) into (7) results in the forcing term

$$-\sigma = (1.6\pi^4 + 0.1)\sin(2\pi x) + 0.7,\tag{A.15}$$

which we apply over a spatial domain of width 1.

Next, we choose an ansatz function for U, which leads us to the compatible solution

$$\mathbf{U} = \frac{0.015}{2\pi + \pi^{-1}} \cos(2\pi x). \tag{A.16}$$

Imposing stress values from equation (A.15), constant coefficients described above, and appropriate boundary conditions, our solver should produce an approximation to equations (A.14) and (A.16) that improves with increasing mesh refinement. Fig. A1 demonstrates the expected quadratic convergence of our linear solver with respect to mesh refinement.

We do not have an analytical solution for the full time-dependent system of equations, but we can solve for crustal thickening at t=0:

$$\dot{h}_{(t=0)} = \frac{0.03\pi}{2\pi + \pi^{-1}} \sin(2\pi x) \tag{A.17}$$

After a single very small time step,  $\delta t$ , our model should converge on the first order approximation

$$\dot{h}_{(t=\delta t)} \approx 1 + \delta t \frac{0.03\pi}{2\pi + \pi^{-1}} \sin(2\pi x).$$
 (A.18)

Convergence with equation (A.18) is demonstrated in Fig. A1. Deviation from a simple convergence line can be seen for high mesh resolution, because of inaccuracy introduced by only considering a first-order approximation to the exact solution.

#### A3 Time stepping

The backwards Euler scheme applied in equation (A.3) is stable for large time steps, but overshoots are possible, and time discretization must be good enough to capture the dynamics of changing overburden stresses. Time step size  $\Delta t$  is chosen to satisfy a Courant-Friedrichs-Lewy (CFL) condition

$$\Delta t = C \min \left( \frac{2R_K}{||\chi||_{L^{\infty}(\Omega_K)}} \right)$$
 (A.19)

where  $R_K$  denotes the radius of cell K.  $||\chi||_{L^{\infty}(\Omega_K)}$  denotes the  $L^{\infty}$  norm of local rates of change over cell K, calculated as the maximum of either the fluid flow velocity  $\mathbf{U}$ , or crustal thickening  $\dot{h}$ . We set the stabilization parameter C=1.0 to balance computation efficiency and numerical stability, while providing sufficient temporal resolution to capture changes in external forcing.